

See discussions, stats, and author profiles for this publication at: <https://www.researchgate.net/publication/258953656>

# Electrochemical Single-Molecule Detection in Aqueous Solution Using Self-Aligned Nanogap Transducers

ARTICLE *in* ACS NANO · NOVEMBER 2013

Impact Factor: 12.88 · DOI: 10.1021/nn404440v · Source: PubMed

---

CITATIONS

17

---

READS

73

## 5 AUTHORS, INCLUDING:



Klaus Mathwig

University of Groningen

35 PUBLICATIONS 272 CITATIONS

[SEE PROFILE](#)



Dileep Mampallil

19 PUBLICATIONS 163 CITATIONS

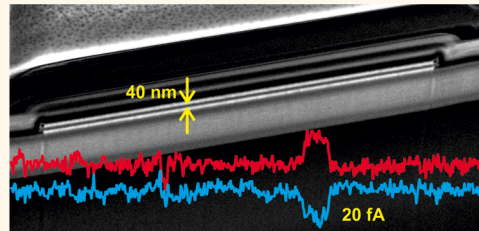
[SEE PROFILE](#)

# Electrochemical Single-Molecule Detection in Aqueous Solution Using Self-Aligned Nanogap Transducers

Shuo Kang, Ab F. Nieuwenhuis, Klaus Mathwig, Dileep Mampallil, and Serge G. Lemay\*

MESA+ Institute for Nanotechnology, University of Twente, PO Box 217, 7500 AE Enschede, The Netherlands

**ABSTRACT** Electrochemical detection of individual molecular tags in nanochannels may enable cost-effective, massively parallel analysis and diagnostics platforms. Here we demonstrate single-molecule detection of prototypical analytes in aqueous solution based on redox cycling in 40 nm nanogap transducers. These nanofluidic devices are fabricated using standard microfabrication techniques combined with a self-aligned approach that minimizes gap size and dead volume. We demonstrate the detection of three common redox mediators at physiological salt concentrations.



**KEYWORDS:** single-molecule detection • electrochemistry • aqueous solution • nanofluidics • self-aligned • nanogap • redox cycling

Techniques for detecting and manipulating (macro)molecules in solution near or at the single-molecule limit enable both fundamental studies and new analytic applications.<sup>1–7</sup> The latter include assays in which the sample has a microscopic volume, such as single-cell analysis,<sup>8,9</sup> or in which the measurement inherently requires such resolution, for example single-molecule DNA sequencing.<sup>10</sup> Particularly interesting are purely electrical detection approaches that are compatible with integrated electronics, as they can lead to massively parallel assays at low costs, enabling faster and cheaper point-of-care diagnostic<sup>11,12</sup> and clinical tools.<sup>13</sup> An important bottleneck in the development of such technology is the realization of transducers that can effectively convert chemical information directly into electrical signals at micro- and nanoscale detectors.

A candidate approach is electrochemical detection, an all-electrical, low-power transduction mechanism that is highly compatible with microfabrication. We recently demonstrated electrochemical single-molecule detection at the proof-of-concept level in an organic solvent, acetonitrile, using nanogap devices.<sup>14</sup> These consist of two closely spaced electrodes separated by a nanochannel, as sketched in Figure 1a. Redox cycling—the repeated, successive oxidation and reduction of analyte molecules

at the two electrodes—provided the required charge amplification.

Even with highly efficient redox cycling, however, single-molecule detection is characterized by extremely low current levels in the femtoampere ( $10^{-15}$  A) range. This is near the limits of detectability at room temperature. As a result, and because the diffusion coefficient of redox molecules in water is lower than that in typical organic solvents, measurements in water have proven unsuccessful so far. Since most (bio)analytical samples take the form of aqueous solutions, the ability to measure in water represents a key milestone in the further development of single-molecule electrochemical assays.

Here we present the first nanofluidic single-molecule electrochemical measurements in aqueous solution. This is made possible by a new microfabrication approach based on a self-aligned process that refines the nanogap geometry (eliminating the so-called dead volume illustrated in Figure 1b) and facilitates downscaling the gap size. This process is based entirely on conventional optical lithography and is thus suitable for mass production. We demonstrate the ability to detect common redox mediators including ferricyanide and ferrocene derivatives as they freely diffuse in and out of the detection region of the transducer, as illustrated in Figure 1c. All

\* Address correspondence to  
S.G.Lemay@utwente.nl.

Received for review August 25, 2013  
and accepted November 26, 2013.

Published online November 26, 2013  
10.1021/nn404440v

© 2013 American Chemical Society

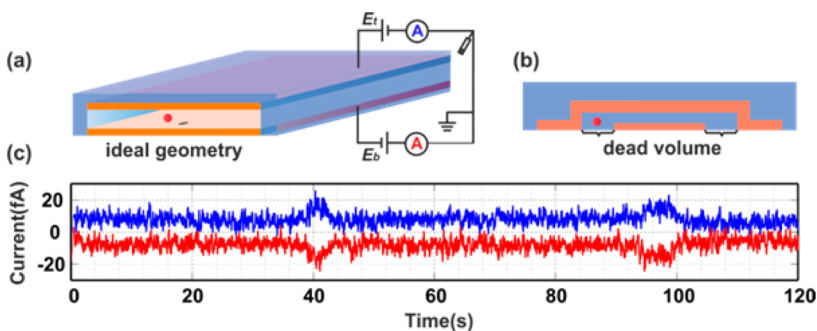


**Figure 1.** (a) Schematic of a nanogap device with ideal geometry: both the top and bottom electrodes span the full width of the nanochannel. (b) Schematic cross-section of a nanogap device with dead volumes due to alignment tolerances during microfabrication. This lowers the redox-cycling efficiency. (c) Current–time traces simultaneously obtained at the top (blue) and bottom (red) electrodes under redox cycling conditions ( $E_t = 0.5$  V and  $E_b = 0.35$  V with 10 pM FcTMABr in 0.1 M KCl aqueous solution). The traces have been vertically offset for clarity. Discrete, anticorrelated current steps with amplitude  $\sim 7$  fA are generated each time that an individual FcTMA<sup>+</sup> molecule enters and subsequently exits the nanogap. Here two events are observed during a 120 s period.

measurements were performed near physiological conditions, illustrating the compatibility of our approach with samples of biological relevance.

## RESULTS AND DISCUSSION

**Self-Aligned Electrode Fabrication.** A key challenge in fabricating nanogaps is to minimize the distance between the electrodes,  $z$ , while avoiding short circuits along the edges of the electrodes. In earlier work,<sup>15–17</sup> the bottom electrode, a sacrificial layer, and the top electrode were deposited in separate steps with the sacrificial layer completely enveloping the bottom electrode in order to prevent any contact between the top and bottom electrodes. Following removal of the sacrificial layer this led to the geometry shown in Figure 1b, where the electrode spacing  $z$  is set by the original thickness of the sacrificial layer. As the thickness of the sacrificial layer must be thicker than that of the bottom electrode to guarantee good step coverage, this imposed an important limitation on the minimum achievable  $z$ . In addition, the sacrificial layer needed to be wider than the bottom electrode to allow for alignment tolerances during lithography. This in turn led to a dead volume where the top and bottom electrodes did not overlap, as indicated in Figure 1b. Whenever an analyte molecule enters this region, no redox cycling can take place, lowering the observed current. Given typical alignment tolerances in optical lithography, the dead volume can easily be as wide as 1  $\mu\text{m}$  on each side of the bottom electrode, thus occupying 40% of the channel in a 5  $\mu\text{m}$  wide device<sup>16</sup> and causing a corresponding decrease in the single-molecule signal. Because single-molecule detection is at the limit of the sensitivity of present electronics, this can be enough to render such measurements impossible.

Here we introduce an alternate approach that circumvents these difficulties. The bottom electrode, sacrificial layer, and top electrode were first deposited together, following which the edges of the electrodes and sacrificial layer were defined in a single lithography

step. This allowed both minimizing the dead volume and simultaneously reducing the risk of short circuits between the electrodes. An additional benefit was that the electrode surface was not exposed to environmental conditions or additional chemicals throughout the complete fabrication process up to release of the sacrificial layer. Such an uncontaminated surface can improve the reproducibility of electrochemical measurements, which are very sensitive to surface conditions.

Figure 2a shows an optical image of a finished device, and the fabrication scheme is illustrated in Figure 2b. In short, a stack of metal layers was deposited and patterned in one step on a 4 in. Si wafer (step 1), followed by an ion-beam etching (IBE) to define the detection region with SiO<sub>2</sub> as a mask (steps 2 and 3). Step 3 represents the key step in creating the “self-aligned” structure, as it automatically leads to the sacrificial layer and top electrode having the same width independently of alignment tolerances. Step 3 was also followed by a short (5 min) cleaning etch in aqua regia to remove material redeposited during IBE. Afterward (steps 4–7) another metal layer stack was defined as the electrical interconnection for the top electrode between two passivation layers deposited as insulating and protecting layer, and finally access holes were generated through which the sacrificial layer was etched and the nanochannel was released (steps 8 and 9). Additional details about the individual steps are given in the Methods section.

Figure 3a shows a scanning electron microscope (SEM) image of a finished device, while Figure 3b–d show its cross sections at different levels of magnification after the device was cut open using a focused ion beam (FIB) along the dashed line in Figure 3a. A 200 nm wide dead-volume region is visible on each side of the bottom electrode, as indicated by the dotted lines in Figure 3d; this was created during the cleaning aqua regia etch, which also attacked the edge of the top electrode. Further optimizing the durations of the IBE

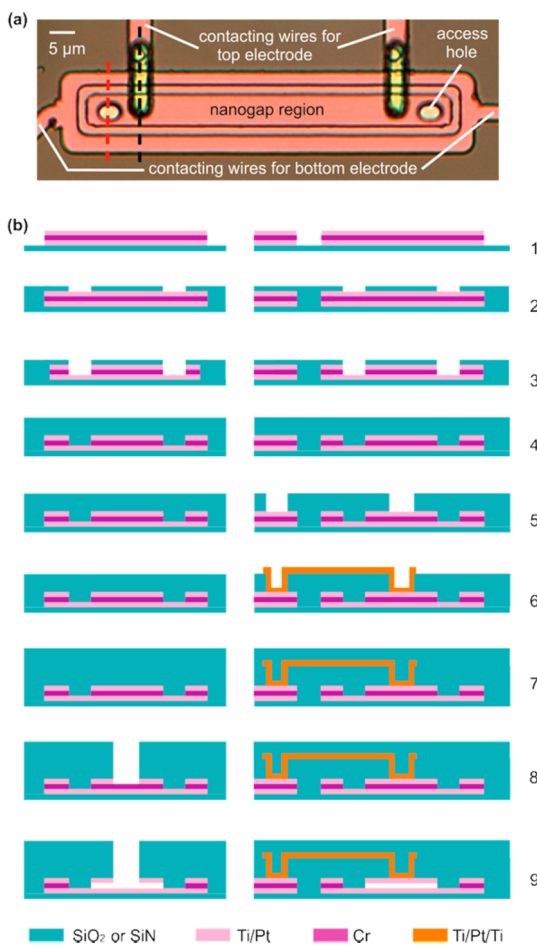


**Figure 2.** (a) Optical microscope image (top view) of a device prior to Cr etching. (b) Schematic device cross sections (not drawn to scale) at different stages of the fabrication process; the sketches in the left and right columns correspond to the cross sections along the red and black dashed lines in (a), respectively. 1. A stack of metal layers is deposited and patterned. 2. SiO<sub>2</sub> is deposited and patterned as a mask layer. 3. A trench is etched by IBE to define the detection region, and treatment in aqua regia is used to remove the redeposition. 4 and 5. SiN is deposited and patterned. 6. A metal layer stack is deposited and patterned for electrical interconnection. 7. A final passivation layer is deposited. 8. Access holes are generated. 9. The sacrificial layer is etched, and the nanochannel is released.

and aqua regia etches (see Supporting Information) allowed compensating for this unwanted feature, resulting in a dead volume as small as 80 nm (Figure 3e).

The morphology of the device was measured with atomic force microscopy (AFM) to investigate the flatness of the top wall of the electrode once the nanochannel was released and filled with 1 mM Fc-(MeOH)<sub>2</sub> in 0.1 M KCl (AFM image shown in Supporting Information). No bending of the top electrode membrane was observed, as expected since a combination of multiple SiO<sub>2</sub> and SiN layers were deposited to balance the stress.<sup>18,19</sup> Therefore, the gap size solely depends on the thickness of the sacrificial layer.

**Single-Molecule Detection in Aqueous Solution.** Single-molecule detection experiments were based on

amperometry under redox cycling conditions in the presence of a concentration  $C = 10 \text{ pM}$  of redox species; the number of analyte molecules in the detection region is then on average  $\langle N \rangle = CVN_A = 0.06$ , where  $V = 1 \times 10^{-17} \text{ m}^3$  is the volume of the nanochannel between the two electrodes and  $N_A$  is Avogadro's number. Figure 1c illustrates the results of this measurement in the form of current–time traces that were recorded simultaneously through the two electrodes of a nanogap transducer filled with an aqueous solution of 10 pM (ferrocenylmethyl)trimethylammonium bromide (FcTMABr) in 0.1 M KCl. The top and bottom electrodes were biased at potentials of  $E_t = 0.5 \text{ V}$  and  $E_b = 0.35 \text{ V}$ , respectively. Because the formal potential for FcTMA<sup>+</sup> is  $E^{\circ'} = 0.43 \text{ V}$ , the given potentials correspond to oxidizing and reducing potentials, respectively, thus enabling redox cycling. The traces mostly exhibit a background current that is constant within the noise level determined by the measurement electronics. At randomly occurring intervals, however, anticorrelated step-like features are observed in the current. Each of these events corresponds to a single molecule entering the active region by Brownian motion, shuttling  $\sim 10^5$  electrons from the bottom to the top electrode by redox cycling and exiting the active region again.<sup>14</sup> The opposite signs for the steps observed at the top and bottom electrodes correspond to oxidizing and reducing currents, respectively, as expected (additional control experiments supporting our conclusion that the steps originate from single-molecule fluctuations are given in the Supporting Information).

We note that it would be practically impossible to detect an analyte concentration as low as 10 pM by cyclic voltammetry—even with the help of efficient redox-cycling amplification provided by nanogaps—because the corresponding fA-level currents would be dwarfed by unwanted background reactions involving water and oxygen. It is the step-like, discrete nature of the single-molecule events that allows extracting their contribution from the background currents.

The current per molecule in Figure 1c, which corresponds to the height of the single-molecule current plateaus, is observed to be  $\sim 7 \text{ fA}$ . This corresponds to a signal-to-noise ratio (SNR) of 2.3, where we define the SNR as the ratio of the current step height to the standard deviation of the measured background current. How does this measured step height compare to theoretical expectations? In the presence of excess supporting electrolyte, as is the case here, mass transport of the analyte molecules is purely diffusive, and the current per molecule,  $i_p$ , has the general form

$$i_p = i_{p,\text{ideal}} \chi_{\text{bias}} \chi_{\text{geom}} \chi_{\text{ads}} \quad (1)$$

Here  $i_{p,\text{ideal}}$  represents the maximum expected current for pure diffusion and has the value  $i_{p,\text{ideal}} = e/2\tau$ , where  $-e$  is the electron charge,  $\tau = z^2/2D$  is the

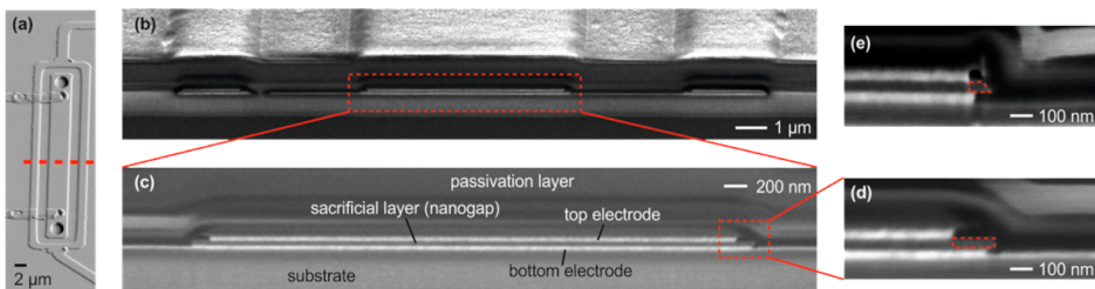


**Figure 3.** Scanning electron microscopy images from a 52° viewing angle. (a) Image of a complete device. (b, c, and d) Cross sections at different magnifications. The device was cut open using a focused ion beam along the line indicated by the dashed line in (a). (b) Complete overview, (c) zoom of the nanochannel, and (d) dead-volume region at high magnification. (e) Cross-section of a different device with optimized etching procedure. The areas outlined with red dotted lines in (d) and (e) represent the dead volume.

average time a molecule takes to diffuse across the gap,  $z$  is again the distance between the electrodes, and  $D$  is the diffusion coefficient of the redox species.<sup>20</sup> In the case where the diffusion coefficients of the reduced ( $D_{\text{red}}$ ) and oxidized ( $D_{\text{ox}}$ ) forms are unequal,<sup>21</sup>  $D = 2D_{\text{red}}D_{\text{ox}}/(D_{\text{red}} + D_{\text{ox}})$ . For aqueous solutions of the analytes studied here the difference between  $D_{\text{ox}}$  and  $D_{\text{red}}$  is however small, and we ignore it for simplicity.  $\chi_{\text{bias}}$ ,  $\chi_{\text{geom}}$ , and  $\chi_{\text{ads}}$  are dimensionless numerical coefficients that represent the signal reduction from the electrode bias, the device geometry (in particular any dead volume), and analyte adsorption to surfaces in the device, respectively:

- The value of  $\chi_{\text{bias}}$  is given, under the assumption of Nernst equilibrium at the two electrodes,<sup>22</sup> by

$$\chi_{\text{bias}} = \left| \frac{1}{1 + e^{-e(E_t - E^{\prime})/kT}} - \frac{1}{1 + e^{-e(E_b - E^{\prime})/kT}} \right| \quad (2)$$

Here  $k$  is the Boltzmann constant,  $T$  is the absolute temperature, and the potentials are as defined above. Deviations are possible due to the finite rate of electron transfer at the electrodes, but this is only a small correction for the fast redox couples employed here.<sup>15</sup> In principle one can always ensure that  $\chi_{\text{bias}}$  has its maximum value of unity by applying sufficient reducing and oxidizing overpotentials at the two electrodes. With analyte concentrations as low as 10 pM, however, it is extremely difficult to remove all background contaminants, so a narrower potential window (100–150 mV) was usually employed to minimize any potential interference from such contaminants. In practice,  $\chi_{\text{bias}}$  was determined from the cyclic voltammogram measured with a 5 μm radius ultramicroelectrode in a 1 mM analyte solution in 0.1 M KCl.

- The value of  $\chi_{\text{geom}}$  represents the fact that shuttling time is lost when an analyte molecule enters the dead volume, effectively reducing the current per molecule (as shown in the Supporting Information). For linear, channel-shaped devices

as discussed here, its value is simply given by the ratio of the width of the active region to the width of the fluid-filled nanochannel; for devices with minimal dead volume, such as that shown in Figure 3e, it has a value  $\chi_{\text{geom}} = 0.97$ .

- Because of the high surface-to-volume ratio of nanogap devices, adsorption can play a large role.<sup>16,23–25</sup> The value of  $\chi_{\text{ads}}$  is given by  $\chi_{\text{ads}} = (1 + \tau_{\text{ads}}/t)^{-1}$ , where  $\tau_{\text{ads}}$  represents the average time per half-cycle spent by an analyte molecule adsorbed to the electrodes.

For the case of Figure 1c, where  $D = 5.0 \times 10^{-6} \text{ cm}^2/\text{s}$  and  $z = 40 \text{ nm}$ , eq 1 yields  $i_{\text{p,ideal}} = 50 \text{ fA}$ . Further correcting for  $\chi_{\text{bias}} = 0.90$  and  $\chi_{\text{geom}} = 0.92$  yields an expected current per molecule of 41 fA. This is significantly higher than the observed steps height,  $i_{\text{p}} = 7 \text{ fA}$ , indicating a substantial degree of adsorption with  $\chi_{\text{ads}} = 0.17$ . This corresponds to each molecule spending more than 80% of its time adsorbed at the electrodes. This level of adsorption is typical for ferrocene derivatives in nanogap devices as determined from high-concentration electrochemical spectroscopy methods.<sup>23,24</sup> Single-molecule measurements in acetonitrile also found substantial suppression of the current due to adsorption with  $\chi_{\text{ads}} = 0.32$ .<sup>24</sup> The current per molecule observed here is thus consistent with expectations.

In order to test the broader applicability of single-molecule detection in our nanogaps, we performed detection experiments for two other commonly employed redox mediators, namely, ferrocenedimethanol ( $\text{Fc}(\text{MeOH})_2$ ,  $E^{\prime} = 0.25 \text{ V}$ ) and ferricyanide ( $\text{Fe}(\text{CN})_6^{3-}$ ,  $E^{\prime} = 0.23 \text{ V}$ ). Figure 4a–c show amperometry results for 10 pM  $\text{FcTMABr}$ ,  $\text{Fc}(\text{MeOH})_2$ , and  $\text{K}_3[\text{Fe}(\text{CN})_6]$  in 0.1 M KCl as supporting electrolyte at room temperature (22 °C) under redox conditions ( $E_t = 0.5 \text{ V}$  and  $E_b = 0.35 \text{ V}$  for  $\text{FcTMA}^+$ ,  $E_t = 0.3 \text{ V}$  and  $E_b = 0.2 \text{ V}$  for  $\text{Fc}(\text{MeOH})_2$ ,  $E_t = 0.3 \text{ V}$  and  $E_b = 0.15 \text{ V}$  for  $\text{Fe}(\text{CN})_6^{3-}$ ). In each case events with a height of 5–7 fA were observed. Taking into account the different values of the diffusion coefficient  $D$ ,  $\chi_{\text{bias}}$  and  $\chi_{\text{geom}}$  in each case, as summarized in Table 1, this indicates different degrees

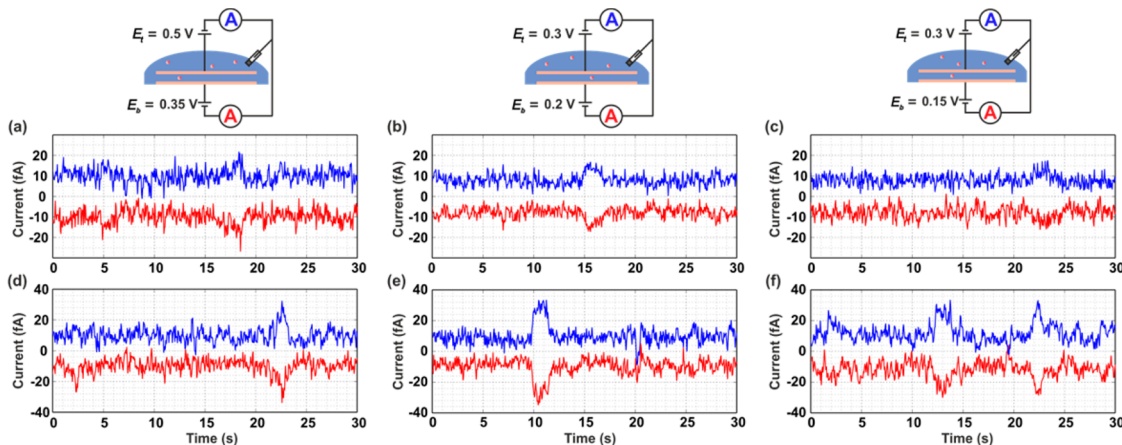


**Figure 4.** Bias schemes and current–time traces for single-molecule detection in (a, d) 10 pM FcTMABr in 0.1 M KCl, (b, e) 10 pM Fe(MeOH)<sub>2</sub> in 0.1 M KCl, and (c, f) 10 pM K<sub>3</sub>Fe(CN)<sub>6</sub> in 0.1 M KCl. The top and bottom rows were measured at 22 and 37 °C, respectively. The traces have been vertically offset for clarity.

**TABLE 1. Theoretical and Measured Values in eq 1 for Single-Molecule Measurements with FcTMA<sup>+</sup>, Fc(MeOH)<sub>2</sub>, and Fe(CN)<sub>6</sub><sup>3-</sup> at 22 and 37 °C**

temperature	quantity	FcTMA <sup>+</sup>	Fc(MeOH) <sub>2</sub>	Fe(CN) <sub>6</sub> <sup>3-</sup>
22 °C	$\chi_{\text{geom}}$	0.92	0.80	0.92
	$\chi_{\text{bias}}$	0.88	0.75	0.88
	$D$ (cm <sup>2</sup> /s)	$5.0 \times 10^{-6}$	$5.6 \times 10^{-6}$	$6.0 \times 10^{-6}$
	$i_p$ (fA, measured)	$5 \pm 1$	$7 \pm 1$	$5 \pm 1$
	$i_{p,\text{ideal}}$ (fA, theory)	50	56	60
	$i_{p,\text{ideal}}\chi_{\text{bias}}\chi_{\text{geom}}$ (fA, theory)	40	34	49
37 °C	$\chi_{\text{ads}}$	$0.13 \pm 0.02$	$0.21 \pm 0.03$	$0.10 \pm 0.02$
	$\chi_{\text{bias}}$	0.87	0.69	0.82
	$D$ (cm <sup>2</sup> /s)	$7.0 \times 10^{-6}$	$7.8 \times 10^{-6}$	$8.4 \times 10^{-6}$
	$i_p$ (fA, measured)	$14 \pm 2$	$20 \pm 2$	$15 \pm 2$
	$i_{p,\text{ideal}}$ (fA, theory)	70	78	84
	$i_{p,\text{ideal}}\chi_{\text{bias}}\chi_{\text{geom}}$ (fA, theory)	56	43	63
	$\chi_{\text{ads}}$	$0.25 \pm 0.03$	$0.47 \pm 0.04$	$0.24 \pm 0.03$

of adsorption for these three compounds. In particular, FcTMA<sup>+</sup> and Fe(CN)<sub>6</sub><sup>3-</sup> show similar degrees of adsorption, with  $\chi_{\text{ads}}$  having a value of 0.12 and 0.10, respectively, while Fc(MeOH)<sub>2</sub> exhibits the least adsorption with  $\chi_{\text{ads}} = 0.21$ .

Because of the large influence of adsorption on the current per molecule, reducing adsorption can cause a significant improvement in  $i_p$  and the SNR. Since spectroscopic measurements indicate reduced adsorption of ferrocene derivatives at higher temperatures (unpublished data based on the technique of refs 23 and 24), we expected that an increase in temperature would result in increased values for  $i_p$ . To test this hypothesis, we performed measurements at elevated temperatures. Amperometry results at 37 °C, while keeping the other parameters identical to those in Figure 4a–c, are shown in Figure 4d–f. A systematic increase of  $i_p$  by a factor of  $\sim 3$  was observed for each measurement, while the background current noise was essentially unchanged. A factor of 1.4 increase in  $i_p$  can be attributed to the increase in the diffusion coefficient, while the remaining factor of 1.5–3 is attributed

to reduced adsorption, consistent with the spectroscopic measurements. The increase of  $i_p$  was accompanied by a shortening of the average duration of the events, which is also consistent with reduced adsorption: the average time for a molecule to diffuse along the channel becomes shorter if it spends less time being immobilized on the electrode.

These experiments demonstrate unambiguously the ability of nanogap transducers to detect individual molecules in water. Naturally, only events with a duration longer than the response time of the measurement electronics can be resolved. Because we relied on Brownian motion to bring molecules in and out of the detection region, however, we expect that many events may be much shorter; such events are not individually recognized but instead appear as noise in the baseline.<sup>14,26,27</sup> In the future we expect that advection of the sample solution through the nanogap transducer can overcome this difficulty.<sup>26–29</sup> In addition, functionalizing the electrode surface to minimize fouling and adsorption could greatly improve the performance and reliability of the transducer.<sup>24,30–32</sup>

## CONCLUSIONS

We have demonstrated a new self-aligned method for the fabrication of nanogap transducers that allows wafer-scale manufacturing of devices with 40 nm electrode spacing and sub-100 nm dead volume using conventional optical lithography with relatively poor ( $1\text{ }\mu\text{m}$ ) alignment tolerances. The resulting gains in redox-cycling efficiency allowed us to detect for the first time

individual redox molecules in aqueous solution using nanofluidic transducers, raising the possibility of new assays based on single-molecule fingerprinting. The robustness of the technique was demonstrated using different common analytes, namely,  $\text{FcTMA}^+$ ,  $\text{Fc}(\text{MeOH})_2$ , and  $\text{Fe}(\text{CN})_6^{3-}$ . It was further shown that the magnitude of the single-molecule signal can be increased by mitigating analyte adsorption.

## METHODS

**Fabrication of Nanogap Devices.** The complete process flow is shown in Figure 2b. In step 1, a stack of metal film layers consisting of 15 nm/50 nm/40 nm/50 nm/10 nm Ti/Pt/Cr/Pt/Ti was defined on a 4 in. Si wafer with 500 nm thermally grown  $\text{SiO}_2$ . The metal layers were deposited consecutively by electron-beam evaporation without breaking vacuum and patterned using a lift-off process based on a positive photoresist (OIR 907-17, Arch Chemicals). Afterward, a layer of 210 nm of plasma-enhanced chemical vapor deposition (PECVD)  $\text{SiO}_2$  was deposited and patterned (step 2) in a RIE etcher to function as the mask for the following ion-beam etching step.

IBE was chosen to etch through the Pt top electrode and Cr sacrificial layer and thus define the active region of the device (step 3). This was because it was found that the etching speed of Cr by wet etching was too fast to control<sup>33</sup> and that RIE deposited contaminants at the edges of the pattern, which were difficult to remove.  $\text{SiO}_2$  was used as mask instead of photoresist because the photoresist was hardened during IBE and difficult to remove afterward. The IBE was done with an Oxford i300 system that has a secondary ion mass spectrometry (SIMS) end point detector integrated in the chamber. Etching was terminated 20 s after a rising signal of Pt was observed in SIMS to guarantee that all the Cr in the trench had been removed. During IBE the wafer was tilted with an ion beam incident angle of  $70^\circ$  and rotated with a speed of 5 rpm. Nonetheless, redeposition<sup>34–36</sup> of some of the etched Cr and Pt was inevitable, resulting in an electrical connection between the two electrodes. The wafer was therefore immediately dipped into 5% HF for 10 s (to remove a passivation layer,<sup>37,38</sup> see Supporting Information) and immersed into freshly prepared aqua regia solution (37% HCl/70%  $\text{HNO}_3/\text{H}_2\text{O}$ , 3:1:2, no external heating) for 5 min to remove the Pt redeposited during IBE.

Subsequently, a passivation layer of 210 nm PECVD SiN was deposited (step 4) to cover all the metal layers. In the next two steps, a contact wire was deposited to provide a connection between the top electrode and its leading wire by first etching through the SiN plus  $\text{SiO}_2$  using RIE so as to open a contact window (step 5) and then lifting off the sputtered 10 nm/340 nm/10 nm Ti/Pt/Ti (step 6) with the same photoresist as used in step 1. A final passivation layer consisting of 108 nm/528 nm/108 nm PECVD  $\text{SiO}_2/\text{SiN}/\text{SiO}_2$  was deposited (step 7) to protect the device from being exposed to the liquid. Finally entrance holes were generated by RIE through the passivation layer followed by IBE through the top Pt layer (step 8). A second 10 s 5% HF dip plus aqua regia treatment of 8 min was carried out to remove any redeposition. Immediately before electrochemical measurements, the Cr layer was etched by immersing the device in Chromium Etch Selectipur (BASF), creating a nanochannel (step 9).

After releasing the nanochannel but before measurements, the devices were placed in a sonication bath and vortex to increase their robustness, since 40 nm long hanging beams of  $\text{TiO}_2$  were generated around the access holes in step 8, causing failures in some devices. By this method, the yield of the devices was 50%. More detailed explanations and information are provided in the Supporting Information.

The devices used for the experiments had a channel dimension of  $50\text{ }\mu\text{m} \times 5\text{ }\mu\text{m} \times 40\text{ nm}$ , with  $4 \times 2\text{ }\mu\text{m}^2$  access holes at each end.

**Electrical Measurements.** The currents were measured with two FEMTO DDPKA-300 variable-gain subfemtoampere amplifiers that were controlled with in-house LabVIEW software. The transimpedance gain was  $10^{12}$  V/A, and oversampling with a sampling frequency of 10 kHz and an averaging interval of 50 ms was employed. In the absence of redox molecules, the current traces exhibited random noise with amplitude 3–5 fA rms. A standard Ag/AgCl electrode (3 M NaCl, BASi) served as both reference and counter electrode. This configuration is appropriate since the current flowing through the reference electrode is negligibly small. The reference electrode was immersed in a PDMS reservoir with an opening at the bottom that contacted the device. All the potentials mentioned in the article are referenced to Ag/AgCl. The device was placed on a vibration isolation table inside a Faraday cage to shield vibration and interfering electrical signals. For the high-temperature measurements, the chip was placed on a copper block that was heated by passing a current generated by a TTI PL303-P power supply through a 20 ohm 50 W resistor glued onto the block. The temperature was monitored with a K-type (Chromel-Alumel) thermocouple reader (206-3738, RS components).

The diffusion coefficients of the analyte molecules were determined from the diffusion-limited current at a  $5\text{ }\mu\text{m}$  radius platinum ultramicroelectrode (BASi MF-2005).

**Chemicals.** (Ferrocenylmethyl)trimethylammonium bromide (FcTMABr) was purchased from ABCR GmbH (cat. no. AB145893), potassium ferricyanide ( $\text{K}_3\text{Fe}(\text{CN})_6$ ) from Sigma-Aldrich (cat. no. 702587), ferrocenedimethanol ( $\text{Fc}(\text{MeOH})_2$ ) from Acros (cat. no. 382550010), potassium chloride (KCl) from Sigma-Aldrich (cat. no. P3911), and Selectipur chromium etchant from BASF. All chemicals were used as received, and the solutions were prepared using  $18.2\text{ M}\Omega\text{ cm}$  Milli-Q water.

**Conflict of Interest:** The authors declare no competing financial interest.

**Acknowledgment.** The authors gratefully acknowledge financial support from The Netherlands Organization for Scientific Research (NWO) and the European Research Council (ERC).

**Supporting Information Available:** Stress-balanced passivation layer and AFM measurement of the morphology of the device, redeposition in IBE, HF pretreatment and etching with aqua regia, hanging beams around the access holes, single-molecule detection control experiments, and ultralow noise current measurements. This material is available free of charge via the Internet at <http://pubs.acs.org>.

## REFERENCES AND NOTES

- Walter, N. G.; Huang, C. Y.; Manzo, A. J.; Sobhy, M. A. Do-It-Yourself Guide: How to Use the Modern Single-Molecule Toolkit. *Nat. Methods* **2008**, *5*, 475–489.
- Hinterdorfer, P.; Van Oijen, A. *Handbook of Single-Molecule Biophysics*; Springer: New York, 2009.
- Walt, D. R. Optical Methods for Single Molecule Detection and Analysis. *Anal. Chem.* **2013**, *85*, 1258–1263.
- Haas, P.; Then, P.; Wild, A.; Grange, W.; Zorman, S.; Hegner, M.; Calame, M.; Aeby, U.; Flammer, J.; Hecht, B. Fast Quantitative Single-Molecule Detection at Ultralow Concentrations. *Anal. Chem.* **2010**, *82*, 6299–6302.

5. Li, W.; Bell, N. A. W.; Hernández-Ainsa, S.; Thacker, V. V.; Thackray, A. M.; Bujdoso, R.; Keyser, U. F. Single Protein Molecule Detection by Glass Nanopores. *ACS Nano* **2013**, *7*, 4129–4134.
6. Rajendran, A.; Endo, M.; Sugiyama, H. Single-Molecule Analysis Using DNA Origami. *Angew. Chem., Int. Ed.* **2012**, *51*, 874–890.
7. Witters, D.; Knez, K.; Ceyssens, F.; Puers, R.; Lammertyn, J. Digital Microfluidics-Enabled Single-Molecule Detection by Printing and Sealing Single Magnetic Beads in Femtoliter Droplets. *Lab Chip* **2013**, *13*, 2047–2054.
8. Kalisky, T.; Quake, S. R. Single-Cell Genomics. *Nat. Methods* **2011**, *8*, 311–314.
9. Yin, H.; Marshall, D. Microfluidics for Single Cell Analysis. *Curr. Opin. Biotechnol.* **2012**, *23*, 110–119.
10. Eid, J.; Fehr, A.; Gray, J.; Luong, K.; Lyle, J.; Otto, G.; Peluso, P.; Rank, D.; Baybayan, P.; Bettman, B.; et al. Real-Time DNA Sequencing from Single Polymerase Molecules. *Science* **2009**, *323*, 133–138.
11. Wang, J. Electrochemical Biosensors: Towards Point-of-Care Cancer Diagnostics. *Biosens. Bioelectron.* **2006**, *21*, 1887–1892.
12. White, R. J.; Kallewaard, H. M.; Hsieh, W.; Patterson, A. S.; Kasehagen, J. B.; Cash, K. J.; Uzawa, T.; Soh, H. T.; Plaxco, K. W. Wash-Free, Electrochemical Platform for the Quantitative, Multiplexed Detection of Specific Antibodies. *Anal. Chem.* **2012**, *84*, 1098–1103.
13. Rothberg, J. M.; Hinz, W.; Rearick, T. M.; Schultz, J.; Mileski, W.; Davey, M.; Leamon, J. H.; Johnson, K.; Milgrew, M. J.; Edwards, M.; et al. An Integrated Semiconductor Device Enabling Non-Optical Genome Sequencing. *Nature* **2011**, *475*, 348–352.
14. Zevenbergen, M. A. G.; Singh, P. S.; Goluch, E. D.; Wolfrum, B. L.; Lemay, S. G. Stochastic Sensing of Single Molecules in a Nanofluidic Electrochemical Device. *Nano Lett.* **2011**, *11*, 2881–2886.
15. Zevenbergen, M. A. G.; Wolfrum, B. L.; Goluch, E. D.; Singh, P. S.; Lemay, S. G. Fast Electron-Transfer Kinetics Probed in Nanofluidic Channels. *J. Am. Chem. Soc.* **2009**, *131*, 11471–11477.
16. Kang, S.; Mathwig, K.; Lemay, S. G. Response Time of Nanofluidic Electrochemical Sensors. *Lab Chip* **2012**, *12*, 1262–1267.
17. Kätelhöön, E.; Hofmann, B.; Lemay, S. G.; Zevenbergen, M. A. G.; Offenhäusser, A.; Wolfrum, B. Nanocavity Redox Cycling Sensors for the Detection of Dopamine Fluctuations in Microfluidic Gradients. *Anal. Chem.* **2010**, *82*, 8502–8509.
18. Faßbender, F.; Schmitt, G.; Schöning, M. J.; Lüth, H.; Buß, G.; Schultz, J. W. Optimization of Passivation Layers for Corrosion Protection of Silicon-Based Microelectrode Arrays. *Sens. Actuators, B* **2000**, *68*, 128–133.
19. Schmitt, G.; Schultz, J. W.; Faßbender, F.; Buß, G.; Lüth, H.; Schöning, M. J. Passivation and Corrosion of Microelectrode Arrays. *Electrochim. Acta* **1999**, *44*, 3865–3883.
20. Fan, F. R. F.; Bard, A. J. Electrochemical Detection of Single Molecules. *Science* **1995**, *267*, 871–874.
21. Mampallil, D.; Mathwig, K.; Kang, S.; Lemay, S. G. Redox Couples with Unequal Diffusion Coefficients: Effect on Redox Cycling. *Anal. Chem.* **2013**, *85*, 6053–6058.
22. Bard, A. J.; Faulkner, L. R. *Electrochemical Methods: Fundamentals and Applications*; John Wiley & Sons: New York, 2001; pp 31–32.
23. Zevenbergen, M. A. G.; Singh, P. S.; Goluch, E. D.; Wolfrum, B. L.; Lemay, S. G. Electrochemical Correlation Spectroscopy in Nanofluidic Cavities. *Anal. Chem.* **2009**, *81*, 8203–8212(1–5).
24. Singh, P. S.; Chan, H. S. M.; Kang, S.; Lemay, S. G. Stochastic Amperometric Fluctuations as a Probe for Dynamic Adsorption in Nanofluidic Electrochemical Systems. *J. Am. Chem. Soc.* **2011**, *133*, 18289–18295.
25. Mathwig, K.; Lemay, S. G. Mass Transport in Electrochemical Nanogap Sensors. *Electrochim. Acta*, in press. DOI: 10.1016/j.electacta.2013.05.142.
26. Singh, P. S.; Katelhon, E.; Mathwig, K.; Wolfrum, B.; Lemay, S. G. Stochasticity in Single-Molecule Nanoelectrochemistry: Origins, Consequences, and Solutions. *ACS Nano* **2012**, *6*, 9662–9671.
27. Lemay, S. G.; Kang, S.; Mathwig, K.; Singh, P. S. Single-Molecule Electrochemistry: Present Status and Outlook. *Acc. Chem. Res.* **2013**, *46*, 369–377.
28. Mathwig, K.; Mampallil, D.; Kang, S.; Lemay, S. G. Electrical Cross-Correlation Spectroscopy: Measuring Picoliter-Per-Minute Flows in Nanochannels. *Phys. Rev. Lett.* **2012**, *109*, 118302(1–5).
29. Mathwig, K.; Lemay, S. Pushing the Limits of Electrical Detection of Ultralow Flows in Nanofluidic Channels. *Micromachines* **2013**, *4*, 138–148.
30. Porter, M. D.; Bright, T. B.; Allara, D. L.; Chidsey, C. E. D. Spontaneously Organized Molecular Assemblies. 4. Structural Characterization of N-Alkyl Thiol Monolayers on Gold by Optical Ellipsometry, Infrared Spectroscopy, and Electrochemistry. *J. Am. Chem. Soc.* **1987**, *109*, 3559–3568.
31. Finkle, H. O.; Avery, S.; Lynch, M.; Furtsch, T. Blocking Oriented Monolayers of Alkyl Mercaptans on Gold Electrodes. *Langmuir* **1987**, *3*, 409–413.
32. Picher, M. M.; Kupcu, S.; Huang, C. J.; Dostalek, J.; Pum, D.; Sleytr, U. B.; Ertl, P. Nanobiotechnology Advanced Anti-fouling Surfaces for the Continuous Electrochemical Monitoring of Glucose in Whole Blood Using a Lab-on-a-Chip. *Lab Chip* **2013**, *13*, 1780–1789.
33. Kelly, J. J.; de Minjer, C. H. An Electrochemical Study of Undercutting during Etching of Duplex Metal Films. *J. Electrochem. Soc.* **1975**, *122*, 931–936.
34. Müller, K. P.; Pelka, J. Redeposition in Ion Milling. *Microelectron. Eng.* **1987**, *7*, 91–101.
35. Chapman, R. E. Redeposition: A Factor in Ion-Beam Etching Topography. *J. Mater. Sci.* **1977**, *12*, 1125–1133.
36. Kinoshita, K.; Utsumi, H.; Suemitsu, K.; Hada, H.; Sugabayashi, T. Etching Magnetic Tunnel Junction with Metal Etchers. *Jpn. J. Appl. Phys.* **2010**, *49*, 08JB02(1–7).
37. Kollensperger, P. A.; Karl, W. J.; Ahmad, M. M.; Pike, W. T.; Green, M. Patterning of Platinum (Pt) Thin Films by Chemical Wet Etching in Aqua Regia. *J. Micromech. Microeng.* **2012**, *22*, 067001(1–6).
38. Kim, M. J.; Gruenke, L. A.; Saia, R. J.; Cohen, S. S. Inhibition of Acid Etching of Pt by Pre-Exposure to Oxygen Plasma. *Appl. Phys. Lett.* **1984**, *44*, 462–464.

**Supporting Information for:  
Electrochemical Single-Molecule Detection in Aqueous Solution using Self-Aligned  
Nanogap Transducers**

Shuo Kang, Ab F. Nieuwenhuis, Klaus Mathwig, Dileep Mampallil and Serge G. Lemay

*MESA+ Institute for Nanotechnology, University of Twente, PO Box 217,  
7500 AE Enschede, the Netherlands*

**A. Reduction of single-molecule current due to dead volume and origin of  $\chi_{\text{geom}}$**

We argue in the main text that the observed single-molecule current,  $i_p$ , is suppressed by a factor  $\chi_{\text{geom}}$  due to the existence of a dead volume. Here we explain in more detail the origin of this suppression.

First consider a particular random-walk trajectory of a molecule in a device with no dead volume, as sketched in Figure S1a. The occupancy of the device increases from 0 to 1 when the molecule enters the active region and returns to 0 when it exits, as sketched in Figure S1b. The corresponding measured redox-cycling current exhibits a similar time evolution, except that, due to the finite response speed of the current measurement circuit, finite rise and fall times are observed. Such limited time resolution is unavoidable: the inverse relationship between the gain and measurement bandwidth of current-detection circuitry ensures that the more sensitive a measurement system, the lower its time resolution. In particular, the rise time of the transconductance amplifiers employed in this work is 350 ms for the  $10^{12}$  V/A gain required for measuring single-molecule signals; only events lasting longer than this can be resolved.

Now consider the same trajectory in a device with a dead volume along both lateral edges of the device, as shown in figure S1d. Each time that the molecule enters the dead volume the occupancy of the active region drops to 0, leading to rapid consecutive oscillations as the molecule travels along the channel (Figure S1e). If the dead volume is sufficiently narrow, however, these random excursions into the dead volume are short-lived compared to the rise time of the electronics. Consequently, the extra fluctuations cannot be resolved and are instead averaged over, as sketched in Figure S1f. Because the total amount of charge transferred per unit time is lowered, however, the fluctuations still result in a decrease in the average detected current. This can be put on a more quantitative footing by noting that the residence time in the dead volume is of order  $\Delta x^2/D$ , where  $\Delta x$  is the width of the dead volume. This corresponds to  $\sim 1$  ms for  $\Delta x = 1 \mu\text{m}$  and decreases rapidly with decreasing dead volume, the typical residence time being thus orders of magnitude shorter than the time resolution for all values of  $\Delta x$  investigated here.

The arguments above are addressed formally in the Supporting Information of Ref. [1]. There we showed analytically that the fluctuations associated with a random process much more rapid than the longitudinal diffusion time scale have negligible effect on the noise spectral density of the redox-cycling signal but do reduce the current per molecule.

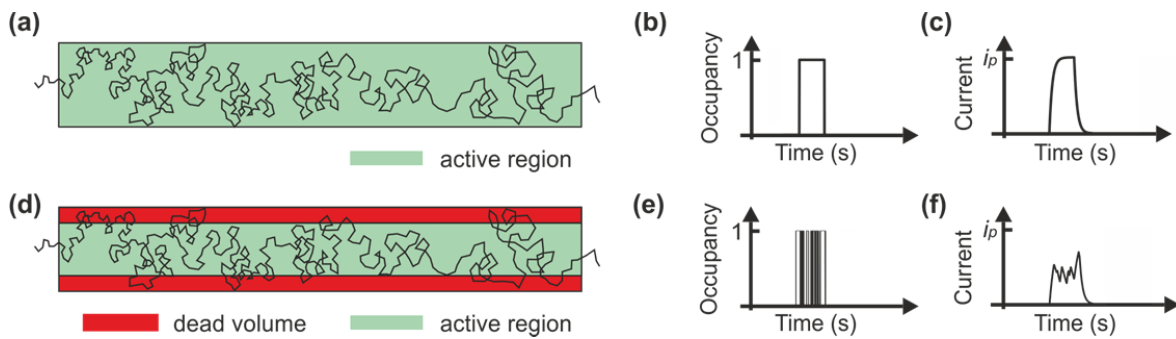


**Figure S1.** (a,d) Sketch of a trajectory of the random walk of a molecule in the plane parallel to the electrode plates in a device without and with dead volume, respectively. (b, e) Simulated occupancy-time traces corresponding to situation (a) and (d). (c, f) Corresponding current-time plot after convolving the trace in (b) and (e) with a model impulse response with a time constant  $\tau$  equal to the rise time of the electronics.

### B. Stress-balanced passivation layer and AFM measurement of the morphology of the device

The complete passivation layer consisted of SiO<sub>2</sub>/SiN/SiO<sub>2</sub>/SiN/SiO<sub>2</sub> 60/210/108/528/38 nm; the bottom and top SiO<sub>2</sub>, which were originally 210 nm and 108 nm as deposited, were later consumed during the IBE (10 nm/min) and 5% HF dip (4 nm/s). A combination of PECVD oxide and nitride was employed because a layer with tensile stress was required to prevent film bending<sup>2</sup> and, based on previous reports, multiplex layers exhibit superior insulation compared to monolayers of pure silicon nitride and silicon dioxide.<sup>3-4</sup>

A device with the nanochannel released was placed in an atomic force microscope (AFM, Cypher, Asylum Research) liquid cell that was filled with 1 mM Fc(MeOH)<sub>2</sub> in 0.1 M KCl and the morphology was measured in solution in contact mode. The height image and 3D image are shown in Figure S2a and S2b, respectively, which show that the top electrode membrane remained flat.

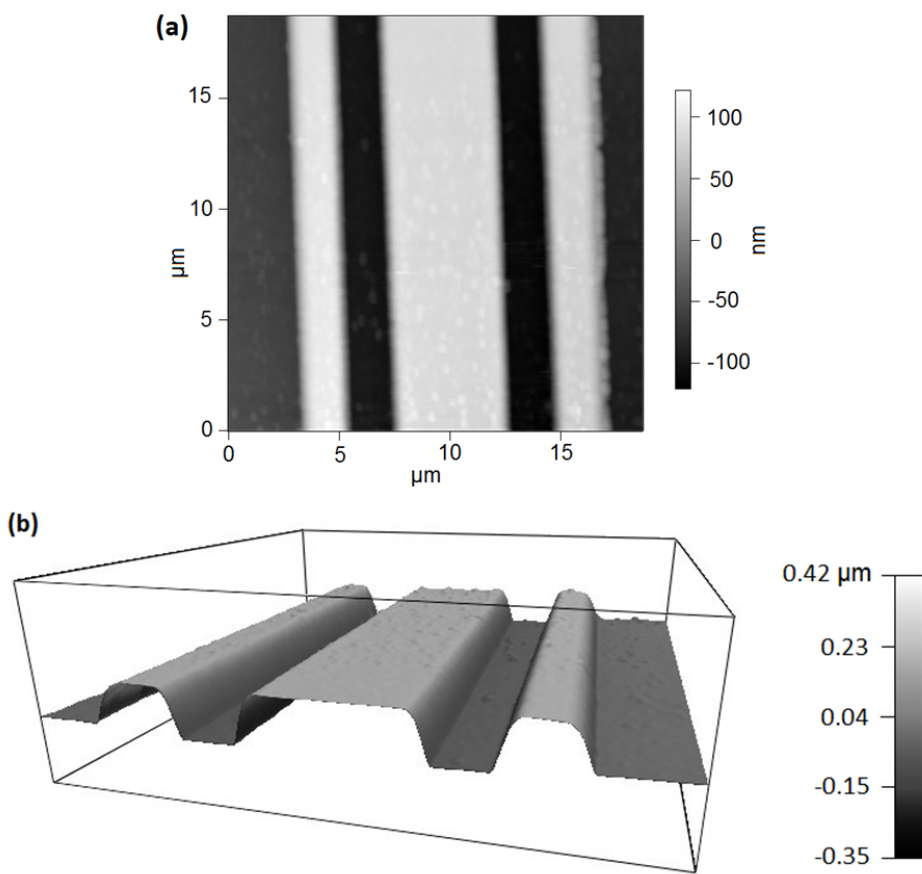


**Figure S2.** AFM images of the detection region of a device. (a) Height image. (b) 3D image.

### C. Redeposition in IBE, HF pre-treatment and etching with aqua regia

To determine the etching rate of the metals in aqua regia (37% HCl : 70% HNO<sub>3</sub> : H<sub>2</sub>O 3 : 1 : 2, no external heating), a test wafer was fabricated following the same method as described in the manuscript up to step 3, etching through the top Pt and Cr with IBE. Afterwards, the wafer was broken into pieces, three of which were processed further, one without any pre-treatment, one dipped in 1% HF for 10 seconds and the other in 5% HF for 10 seconds. All three were then immersed into freshly mixed aqua regia solution for 10 min. Finally, each chip was cleaved along the direction perpendicular to the side wall of the pattern and cross sections were observed with SEM.

Figure S3a shows the SEM image of a chip that was not treated with HF. Pt is not etched at all in aqua regia and a re-deposited film is visible along the side wall. Figures S3b and S3c show two different locations on a chip that was dipped in 1% HF before the aqua regia etch; in both figures, the bottom Pt is not etched, however, the top Pt is etched laterally with a different etching rate in the two cases. This shows that the passivation layer<sup>5-6</sup> formed in the trench that stopped the etching of Pt in aqua regia was not effectively removed; the top Pt electrode was etched when aqua regia went through the rift of the re-deposited film along the side wall, and the etching process thus depended on how much the side wall was sealed by the redeposition. Since it is thicker in Figure S3b than in Figure S3c, the lateral etching of the top Pt was more hindered in the former case than in the latter one.

Figure S3d shows a chip that was pre-treated with 5% HF and in which the  $\text{SiO}_2$  mask layer was much thinner; as a result the bottom Pt in the trench was totally etched in aqua regia and an undercut of  $\sim 100$  nm was created, while the top Pt was etched in the lateral direction for  $\sim 200$  nm. This indicates that the passivation layer was removed by the HF, allowing the Pt to be effectively etched in aqua regia. The redeposition was completely removed in this case, as shown in the figure.

Based on the above tests, it was found that the etching rate of Pt in aqua regia was about 10 – 20 nm/min. The etching proceeded faster where there was a thinner re-deposited layer. Cr was not attacked in aqua regia, thus the sacrificial layer was wider than the two Pt electrodes and short circuits were avoided (Figure S3d). The etching rate of Ti in aqua regia was about 3 Å/min, this slow rate insured that some Ti was still remaining after the etching (as also shown in Figure S3d) and the electrical connection to the bottom electrode was not lost.

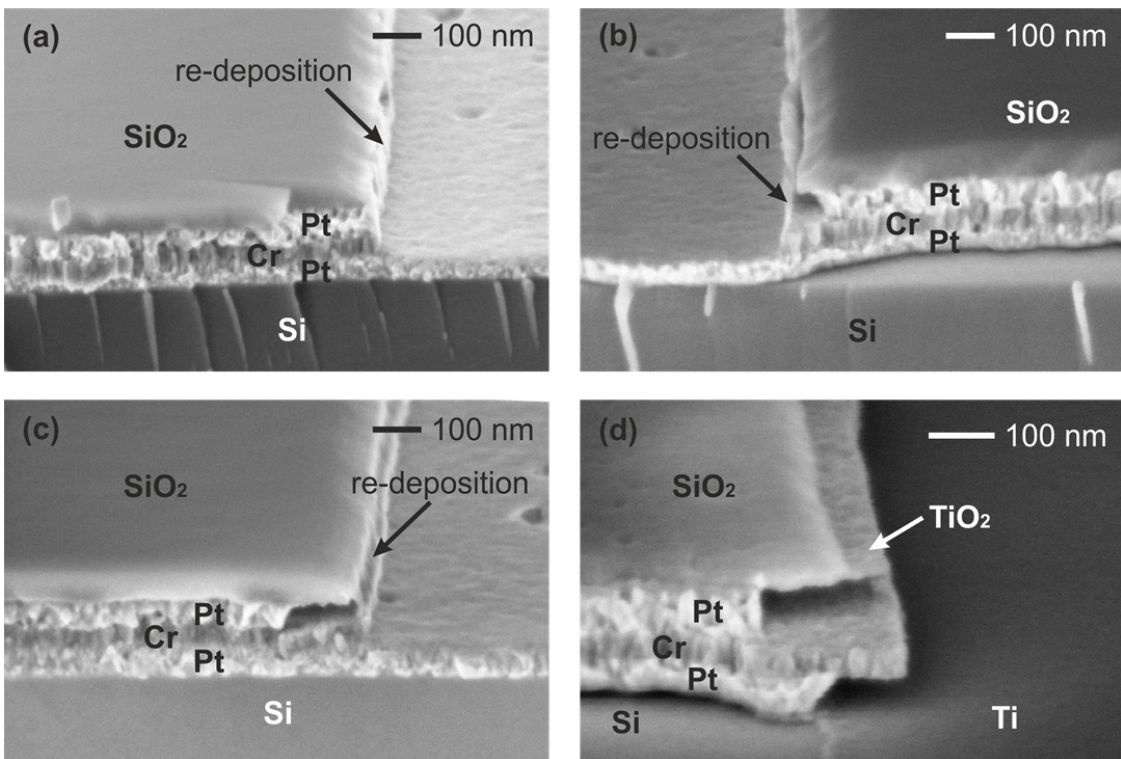


**Figure S3.** Scanning electron microscopy images of cross-sections of test structures immersed for 10 min in aqua regia with (a) no pre-treatment, (b) and (c) 10 s in 1% HF as pre-treatment and (d) 10 s in 5% HF.

In the main article, Figure 3d and 3e show two devices resulted in different geometries by tuning the durations of the IBE and aqua regia etches. The device shown in Figure 3d was fabricated by switching off the IBE as soon as Pt was detected in SIMS, at which point some Cr still remained and hindered the following etching of the Pt beneath. With 20 min etch in aqua regia, the bottom Pt in the trench was still present, and a  $\sim 200$  nm undercut was formed in the top electrode only. In Figure 3e, an over-etching of 20 s was instead employed in the IBE step, etching away all the

Cr in the trench; following 5 min immersion in aqua regia, the bottom electrode was etched through and a further lateral etch proceeded for ~50 nm, while the top electrode was etched laterally for ~80 nm. This represents a good compromise between minimizing the dead volume and, simultaneously, the risk of short circuits.

#### D. Hanging beams around the access holes

In Figure S3d, there is a ~40 nm wide strip hanging at the edge of the remaining SiO<sub>2</sub> mask. This was generated when the Ti adhesion layer of the top Pt electrode was oxidised and became resistant to the etching chemicals. Once the SiO<sub>2</sub> above was etched in 5% HF and the Pt beneath was etched in aqua regia, a hanging beam was formed which was merged with the passivation layer deposited in the following step, causing no risk for later steps. However, beams were also created around the access holes and kept hanging after the 5% HF treatment and aqua regia etching in process step 8. Figure S4a and S4b show the SEM images of access holes of two devices after the nanochannels have been released. In Figure S4a, part of the hanging beam was broken off and flushed away, as indicated by the arrow; this did not influence the functioning of the device. However, if part of the beam collapsed and touched the bottom electrode, a conduction path was formed, as indicated by the arrow in Figure S4b, which caused the failure of the device. Based on a large number of experiments, it was found that the beams could be broken off and the residue flushed away, greatly increasing the robustness of the devices. This was achieved by applying 15 min sonication to the chip (Branson DTH-1510, 42 kHz, 80 W) and subsequently placing the chip in a vortex generated by a magnetic stirrer rotated with a speed of 1600 rpm in a beaker of water. Yields of 50% were achieved with this additional handling. In the future, the formation of hanging beams can be avoided by changing the material used for the IBE mask.

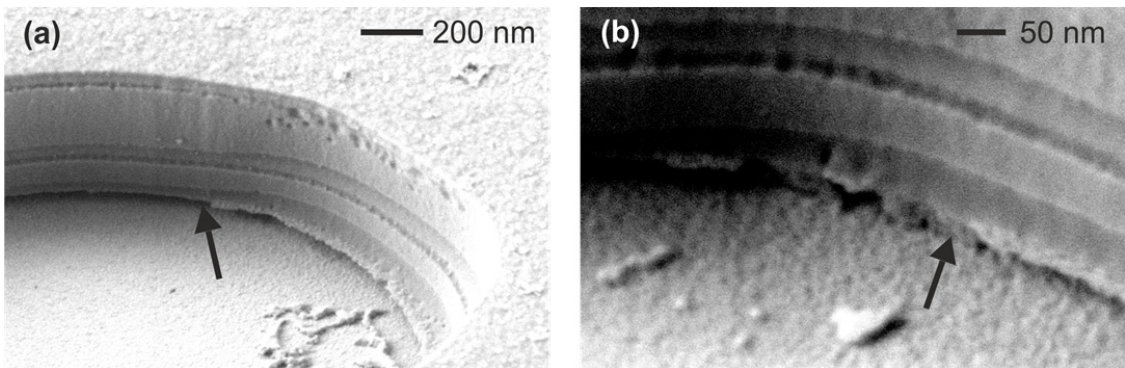


**Figure S4.** Scanning electron microscope images of hanging beams around the access holes. (a) A working device in which part of the hanging beam has been broken off and flushed away. (b) Part of the hanging beam collapses and touches the bottom electrode, forming a conducting path between the top and bottom electrode and causing a short circuit of the device.

#### E. Single-molecule detection control experiments

We interpret the anti-correlated step-like features excused from the baseline as the signature of single molecules entering the nanogap, as further supported by the following control experiments:

- *Measurement at redox cycling conditions with and without redox species.* Figure S5a and S5b show traces obtained from a device biased at  $E_t = 0.48$  V and  $E_b = 0.32$  V in 0.1 M KCl and 10 pM FcTMABr in 0.1 M KCl respectively. By adding FcTMABr, the anti-correlated excursions started to appear, which was not observed with only KCl in the solution. This supports the conclusion that anti-correlated events are caused by the redox molecules.

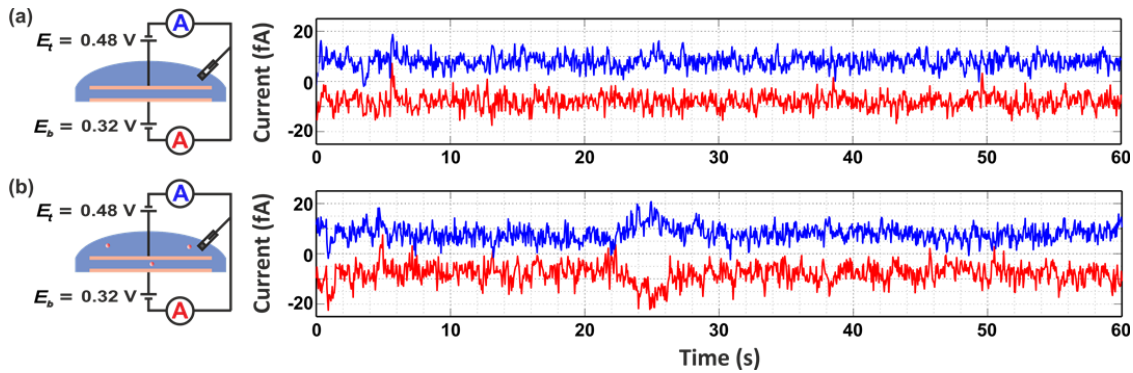


**Figure S5.** Current-time traces at redox cycling conditions ( $E_t = 0.48$  V and  $E_b = 0.32$  V) in (a) 0.1 M KCl and (b) 10 pM FcTMABr in 0.1 M KCl.

- *Measurement in redox species with and without employing redox-cycling potentials.* Figure S6a and S6b show traces measured from a device filled with 10 pM Fc(MeOH)<sub>2</sub> in 0.1 M KCl with  $E_t = E_b = 0.1$  V and  $E_t = 0.3$  V,  $E_b = 0.2$  V respectively. Anti-correlated steps arose only when potentials suitable for redox cycling were applied.

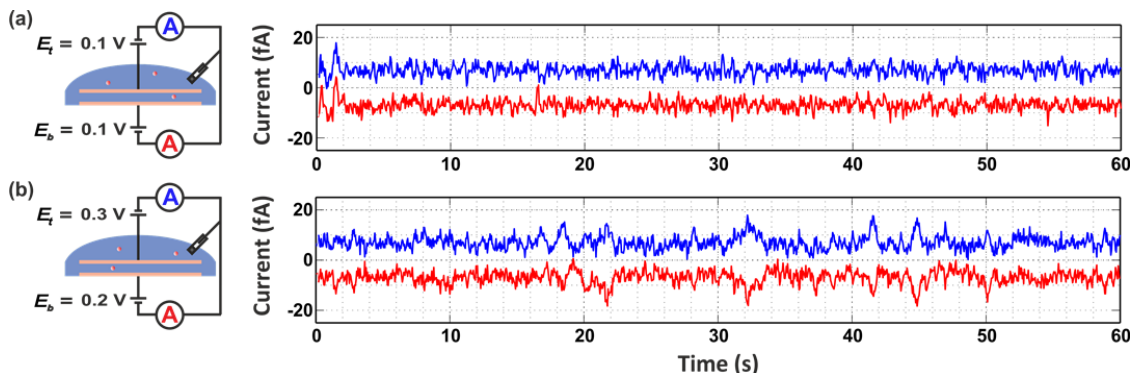


**Figure S6.** Current-time traces measured with 10 pM Fc(MeOH)<sub>2</sub> in 0.1 M KCl at (a)  $E_t = E_b = 0.1$  V and (b)  $E_t = 0.3$  V,  $E_b = 0.2$  V.

- *Measurements while swapping the bias potentials of the electrodes.* Figure S7a and S7b show traces measured in 10 pM Fc(MeOH)<sub>2</sub> in 0.1 M KCl with  $E_t = 0.3$  V,  $E_b = 0.2$  V and  $E_t = 0.2$  V,  $E_b = 0.3$  V, respectively. The polarity of the excursions were reversed when the potentials were swapped, consistent with the reversed oxidizing/reducing role of the electrodes.

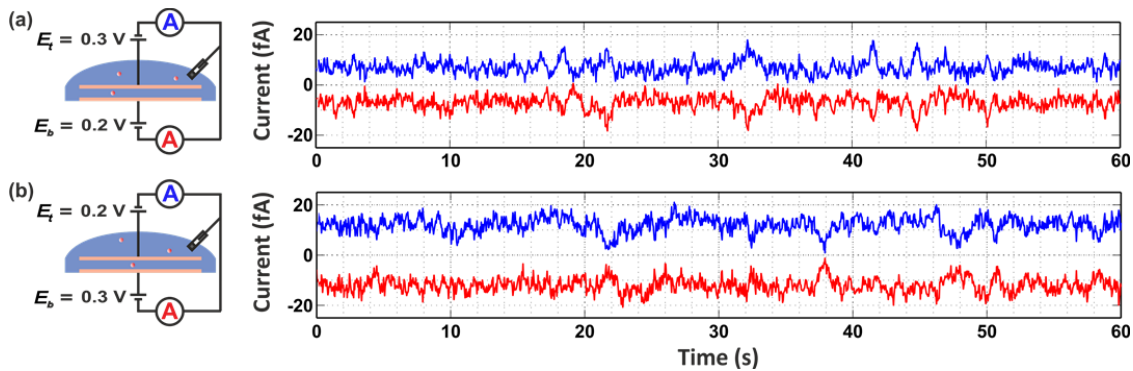


**Figure S7.** Current-time traces measured with 10 pM  $\text{Fc}(\text{MeOH})_2$  in 0.1 M KCl at (a)  $E_t = 0.3 \text{ V}$  and  $E_b = 0.2 \text{ V}$  and (b)  $E_t = 0.2 \text{ V}$ ,  $E_b = 0.3 \text{ V}$ .

- *Measurement with shifted potential window.* Figure S8a and S8b show traces measured from a device filled with 10 pM  $\text{Fc}(\text{MeOH})_2$  in 0.1 M KCl with  $E_t = 0.3 \text{ V}$ ,  $E_b = 0.2 \text{ V}$  and  $E_t = 0.5 \text{ V}$ ,  $E_b = 0.4 \text{ V}$  respectively. When the potential window was shifted to the non-redox cycling region, the signal disappeared.

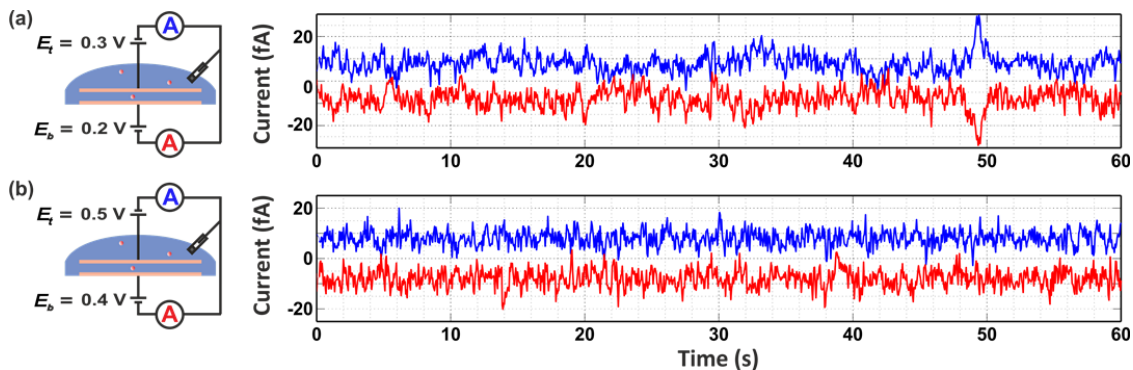


**Figure S8.** Current-time traces measured with 10 pM  $\text{Fc}(\text{MeOH})_2$  in 0.1 M KCl at (a)  $E_t = 0.3 \text{ V}$  and  $E_b = 0.2 \text{ V}$  and (b)  $E_t = 0.5 \text{ V}$ ,  $E_b = 0.4 \text{ V}$ .

- *Cross-correlation analysis of data obtained at different concentrations of  $\text{Fc}(\text{MeOH})_2$  in 0.1 M KCl at  $E_t = 0.4 \text{ V}$  and  $E_b = 0.1 \text{ V}$ .* Each of the two simultaneously acquired amperometric traces consists of two components: the redox cycling current, which has the same magnitude but opposite signs at the two electrodes, and instrumental noise, which is independent for the two electrodes. This allows performance of a cross-correlation analysis<sup>7</sup> to extract the amplitude of the faradaic fluctuations. Figure S9 shows the uncorrelated and anti-correlated parts of the fluctuations in the current versus concentration of  $\text{Fc}(\text{MeOH})_2$ . Noise from the instrumentation is independent of the concentration of redox species, while the faradaic contribution scales as  $C^{1/2}$ , supporting the conclusion that the fluctuations originate from the random walk of the molecules.<sup>6</sup>

At low concentration (100 pM and below), the anti-correlated component shows a higher value than predicted, indicating some contributions from contaminating background signals. At this level, it is extremely difficult to entirely remove contamination, therefore a narrower potential window of 100- 150 mV was employed.

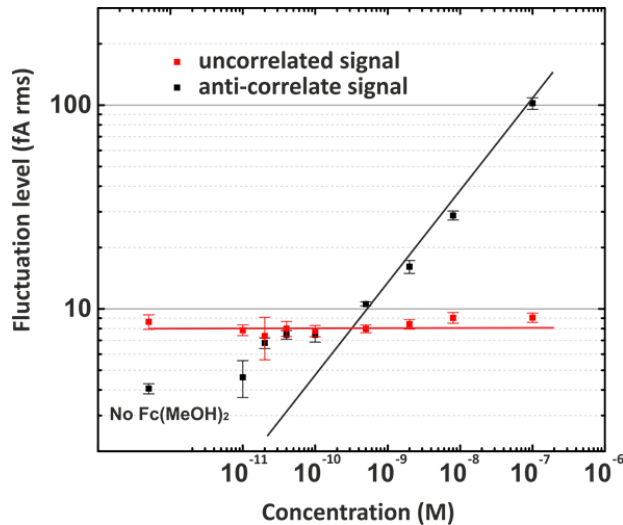


**Figure S9.** Uncorrelated and anti-correlated parts of the measured fluctuations in the current versus concentration of  $\text{Fc}(\text{MeOH})_2$ .

## F. Ultra-low noise current measurements

Together with sub-femto-ampere amplifiers (FEMTO DDPKA-300), a Keithley 7078-TRX low noise triaxial cable was used. The inner shield was driven by a unity gain low impedance amplifier (guard) to reduce the cable leakage current and effective cable capacitance.<sup>8</sup> With probes lifted up to create an open-circuit configuration, the peak-to-peak background noise current with gain settings of  $10^{12}$  and  $10^{13}$  V/A was 2 fA. Part of the measurement setup, including a FEMTO amplifier, triaxial cable and probe manipulator are shown in Figure S10.

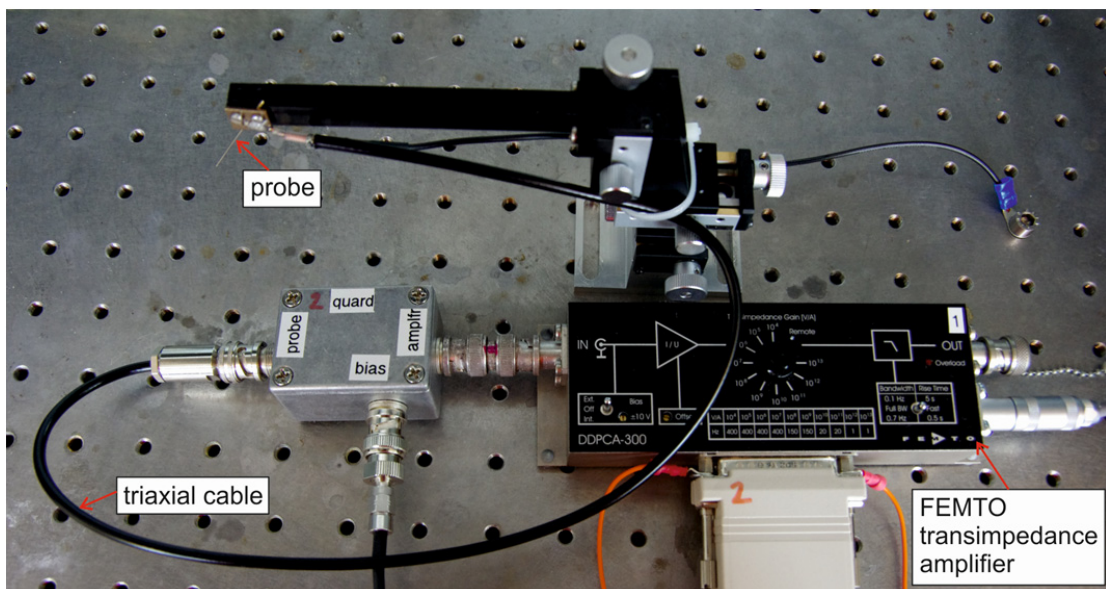


**Figure S10.** Part of the measurement setup, including FEMTO amplifier, triaxial cable, probe manipulator and probe.

## References

1. Zevenbergen, M. A. G.; Singh, P. S.; Goluch, E. D.; Wolfrum B. L.; Lemay S. G. Electrochemical Correlation Spectroscopy in Nanofluidic Cavities. *Anal. Chem.* **2009**, *81*, 8203–8212.
2. Schomburg, W. K. *Introduction to Microsystem Design*; Springer: New York, 2011; pp 41.
3. Schmitt, G.; Schultze, J. W.; Faßbender, F.; Buß, G.; Lüth, H.; Schöning, M. J. Passivation and Corrosion of Microelectrode Arrays. *Electrochim. Acta* **1999**, *44*, 3865-3883.
4. Faßbender, F.; Schmitt, G.; Schöning, M. J.; Lüth, H.; Buß, G.; Schultze, J. W. Optimization of Passivation Layers for Corrosion Protection of Silicon-Based Microelectrode Arrays. *Sens. Actuators, B* **2000**, *68*, 128-133.
5. Kollensperger, P. A.; Karl, W. J.; Ahmad, M. M.; Pike, W. T.; Green, M. Patterning o Platinum (Pt) Thin Films by Chemical Wet Etching in Aqua Regia. *J. Micromech. Microeng.* **2012**, *22*, 067001(1-6).
6. Kim, M. J.; Gruenke, L. A.; Saia, R. J.; Cohen, S. S. Inhibition of Acid Etching of Pt by Pre-Exposure to Oxygen Plasma. *Appl. Phys Lett.* **1984**, *44*, 462-464.
7. Zevenbergen, M. A. G.; Singh, P. S.; Goluch, E. D.; Wolfrum, B. L.; Lemay, S. G. Stochastic Sensing of Single Molecules in a Nanofluidic Electrochemical Device. *Nano Lett.* **2011**, *11*, 2881-2886.
8. Keithley Application Note Series No. 2959.